PERGAMON

Journal of Structural Geology 23 (2001) 1753–1770

JOURNAL OF STRUCTURAL GEOLOGY

www.elsevier.com/locate/jstrugeo

Elastic stress control on the pattern of tensile fracturing around a small fault network at Nash Point, UK

Stephen J. Bourne*, Emanuel J.M. Willemse

Research and Technical Services, Shell International Exploration and Production BV, Rijswijk, The Netherlands

Received 5 June 2000; revised 24 January 2001; accepted 7 February 2001

Abstract

Complex trajectories of fault-related opening-mode fractures at Nash Point in South Wales, UK are consistent with elastic stress fields computed for the observed fault network subject to north–south compression. The linear elasticity theory is used to calculate local stress increments produced by slip on the fault network. Faults are assumed to be free of shear stress and to slip in response to some remote stress load. Brittle failure of rock within this stress field is determined according to a combined Griffith–Coulomb criterion. Discrete fracture networks are simulated according to simple growth rules where fractures initiate according to the state of brittle failure and propagate along a surface normal to the direction of most tensile local stress.

Results demonstrate the dominant opening-mode fracture were caused by a uniform body force (e.g. unloading) and are just locally perturbed by the pre-existing fault network. Fault heights of 2–3 times the mean fault block width, and regional contraction along an azimuth of 180 ± 10° are required to reproduce the observed fracture pattern. Independent kinematic analysis of nearby faults yield estimates of the azimuth of regional contraction of 170–180°. Some features in the observed fracture pattern are not well reproduced but these are small-scale and related to small-scale irregularities on the fault planes.

Keywords: Fracture; Fault; Crack; Dislocation; Geomechanics; Elastic; Stress; Tensile; Body force; Outcrop

1. Introduction

Natural fractures are common in rocks exposed at the Earth's surface, and are known to occur down to depths of several kilometres. At the surface, the spacing, orientation, mechanical strength and aperture of the fractures is important for designing roads, tunnels, dams and other constructions. In the subsurface, the character of natural fracture systems can exert great control over the flow of fluids and gases. Opening-mode fractures may act as highly permeable conduits capable of rapidly transmitting water, oil or gas. Mineralised fractures may compartmentalise reservoirs, or may contain concentrations of valuable ore. Knowledge of the fracture system's geometry and spatial distribution is crucial in understanding the performance, and planning the development, of any fractured reservoir, as well as economically mining various types of ore deposits.

Fractures occur in a variety of geological settings. So-called 'regional joints' exhibit a consistent orientation over very large distances and have been attributed to curvature of the earth (Price, 1966) to burial and uplift cycles (Narr and Currie, 1982; Engelder, 1985), and to crustal plate movements (Hancock, 1985). In other cases, fractures are related to folds (e.g. Harris et al., 1960; Stearns, 1964; Engelder, 1987; Lewis et al., 1990; Lisle, 1994), for example through outer arc extension or layer-parallel slip. In other instances, fracture patterns change orientation and density in the vicinity of faults. Fault slip will tend to generate secondary fractures that propagate away from fault tips (Rispoli, 1981; Willemse and Pollard, 1998), and irregularities of the fault surface (Hyett and Hudson, 1990; Rawnsley et al., 1992), and cause fractures that propagate towards the fault to curve. Because opening-mode fractures grow in the plane of two principal stresses, this suggests that the principal stresses rotate locally to become either parallel or perpendicular to the fault surface. Such near-fault stress rotations are not only inferred from fracture patterns, but also measured directly along major faults (Zoback et al., 1987). These stress rotations suggest the fault surface is not capable of sustaining as significant a shear stress as the surrounding rock.

Fractures form because rock cannot sustain the in-situ stress and are oriented according to the direction of principal stress. Tensile fractures propagate in a surface normal to the

* Corresponding author. Tel.: +31-70-311-6081; fax: +31-70-311-2393.
E-mail addresses: s.j.bourne@siep.shell.com (S.J. Bourne), e.j.m.willemse@siep.shell.com (E.J.M. Willemse).

0191-8141/01/$ - see front matter
PII: S0191-8141(01)00027-X

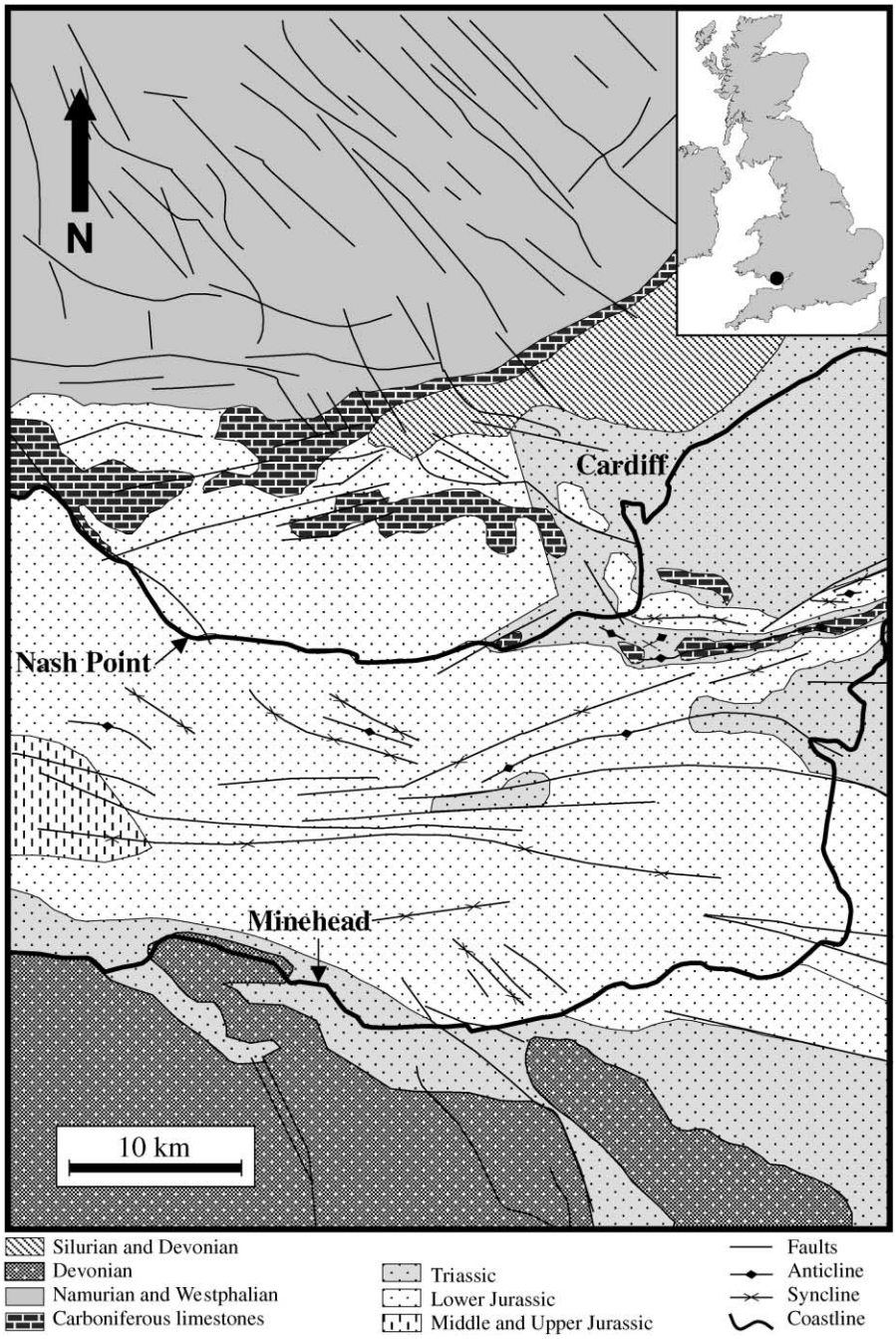

Fig. 1. Location of the Nash Point study area and the main geological features of the eastern Bristol Channel. Based on the British Geological Survey Sheet 51°N–04°W, Bristol Channel.

local direction of maximum tensile stress, and shear fractures propagate in one of the two surfaces parallel to the local direction of the intermediate principal stress and at a fixed angle to the local direction of most compressive stress. Therefore, knowledge of the distribution of stress magnitude and direction throughout a rock body can be used to predict the distribution and orientation of fractures. In general, the state of stress within a rock is the result of many different processes, such as compaction, diagenesis, thermal history, exhumation, tectonic folding and faulting. In this paper, we focus on the last factor and compare complex natural fracture patterns against fairly simple mechanical models in which faults are idealised as cuts in an elastic medium. Where applicable, this method can help to predict fracture networks in the regions adjacent to and between larger-scale faults visible, for example on seismic or satellite images (Bourne et al., 2000). The objectives of this study are: (a) to test the extent to which elastic stress calculations can be used to reproduce the geometry of fault-related fractures, in a case where the actual fault and

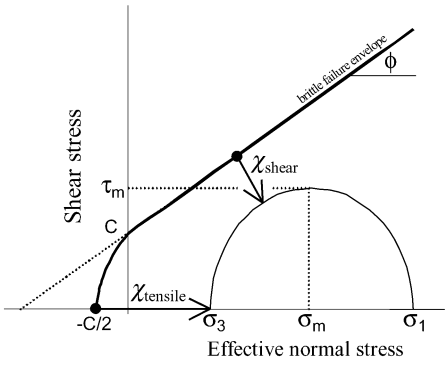

Fig. 2. Proximity of a stress state to brittle failure is represented by the smallest stress increment required to reach that stress state from either the shear failure envelope, χ_{shear}, or the tensile failure envelope, $\chi_{tensile}$.

fracture geometry is known in detail; (b) to define limits on the applicability of elasticity theory to finite deformation around faults; and (c) to understand and limit the sources of error. First, the methodology and mechanical model is described. Subsequently, the model is applied for the case of a single isolated fault and to a fault network as exposed at Nash Point, UK (Fig. 1). Finally, the sensitivity of the results to model parameters is discussed.

2. Methodology to evaluate stress and brittle failure

The calculation of the state of stress and brittle failure around faults requires assumptions regarding the mechanical behaviour of the rocks, a rock failure criterion, a method to compute stress distribution around faults and a set of boundary conditions.

2.1. Force balance

For simplicity we only consider states of static stress equilibrium around faults and thereby neglect any transient stress states that arise during dynamic fault rupture. Equilibrium of forces within the Earth is described by the stress balance equation (Turcotte and Schubert 1982):

$$\frac{\partial \sigma_{ij}}{\partial x_j} = -\rho g \delta_{i3}; \tag{1}$$

given here in indicial notation, where σ_{ij} is the stress tensor, g is the gravitational acceleration, ρ is the density, δ_{ij} is the Kronecker delta, x_3 is directed vertically up, and summation over repeated indices is implied. The internal deformation of a region can be obtained by solving for the distribution of internal stress required to balance a remote load.

As the model must simultaneously represent faults and the surrounding matrix, a constitutive law is required in two parts. One part describes the matrix as a continuum that can fracture, and the other describes faults as displacement discontinuities.

2.2. Constitutive law for matrix

The rock matrix surrounding the faults is described as a homogeneous, isotropic, perfectly elastic-brittle medium. That is, stress states are described by linear elasticity up to the point of first tensile or shear failure. For simplicity, we only consider loads that do not place the majority of the matrix beyond its elastic limit and therefore can neglect any stress relaxation and loss of elastic rigidity caused by small-scale localised fracturing within the matrix. In this context, brittle failure criteria can be applied independently of the stress field calculation.

The elastic relationship between stress and strain is described as:

$$\sigma_{ij} = 2G\epsilon_{ij} + \lambda \epsilon_{kk}\delta_{ij}, \qquad G = \frac{E}{2(1+\nu)}, \qquad \lambda = \frac{E\nu}{(1+\nu)(1-2\nu)}, \tag{2}$$

where G and λ are Lamé coefficients, E is Young's modulus, ν is Poisson's ratio, ϵ_{ij} is the strain tensor, δ_{ij} is the Kronecker delta, and summation over repeated indices is implied.

We adopt the commonly-used Coulomb (1773) and Griffith (1924) criteria to describe the strength envelope for the brittle failure of rock matrix in both shear and tension, respectively. The shear strength of rock is attributed to the presence of internal friction and cohesion on any potential failure surface within the material. The shear strength of a particular failure surface is:

$$\tau = \sigma_n \tan\phi + C, \tag{3}$$

where τ is the shear stress at failure, σ_n is the normal stress across the surface, ϕ is the angle of internal friction, and C is the cohesion (Fig. 2). By convention compressive stresses are positive.

The tensile strength of rock is considered to be governed by the presence of microscopic open cracks, which propagate under stress conditions described by the failure envelope:

$$\tau^2 = 2C\sigma_n + C^2. \tag{4}$$

The proximity of any prevailing stress state to either tensile or shear failure can be described by a stress quantity, χ. In Fig. 2, χ corresponds to the shortest distance from the failure envelope, which represents rock strength, to a Mohr circle (Mohr, 1900; 1914), which represents the initial stress state. Brittle failure occurs if the Mohr circle touches the failure envelope, i.e. $\chi = 0$, and the mode of failure is determined by whichever failure condition is met first; either $\chi_{shear} = 0$ or $\chi_{tensile} = 0$. We choose to represent initially stable stress states, i.e. those below the failure envelope, with negative values of χ. Therefore, from Eqs. (3) and (4), the initial proximity of a stress state to shear and tensile

failure and can be written as:

$$\chi_{\text{shear}} = \tau_{\text{m}} - \sigma_{\text{m}}\sin\phi - C\cos\phi, \tag{5}$$

and

$$\chi_{\text{tensile}} = \tau_{\text{m}} - \sigma_{\text{m}} - \tfrac{1}{2}C, \tag{6}$$

where σ_{m} is the initial mean stress $(\sigma_1 + \sigma_3)/2$, and τ_{m} is the initial maximum shear stress $(\sigma_1 - \sigma_3)/2$, and σ_1 and σ_3 are the most and least compressive effective principal stresses, respectively. Note that the above shear failure proximity is similar, but not identical, to the conventional Coulomb failure stress $(\tau_{\text{m}} - \sigma_{\text{m}}\tan\phi)$ and contains both normal and shear components of stress.

Transition from a stable to a failed state requires an increase in χ such that $\chi \geq 0$. For both tensile and shear failure, this requires an increase in shear stress, or a reduction in mean compressive stress. However, tensile and shear failure may also result from a reduction in internal friction or cohesion. A relatively stable initial stress state will have a large negative χ, whereas a near critical stress state will have a small negative χ.

In linear elastic models, the fields of stress in equilibrium with a constant remote load before and after fault slippage will be different. This consequently represents a change in failure proximity, $\Delta\chi$, from the initial value, χ. Hence, a stress state after fault slippage will be in brittle failure if the criterion

$$\chi + \Delta\chi \geq 0 \tag{7}$$

is satisfied. This model allows computed stresses to exceed tensile and shear rock strengths, disguising the mode of first failure. In this case, failure will have occurred at some intermediate stress between the initial and final stress states. Because linear elasticity is assumed, such an intermediate failure stress can be written as a linear combination of the initial and final stress states, e.g.

$$\sigma_{\text{m}}^{\text{failure}} = \left(1 - \frac{\chi}{\Delta\chi}\right)\sigma_{\text{m}}^{\text{initial}} + \frac{\chi}{\Delta\chi}\sigma_{\text{m}}^{\text{calc}},$$

and

$$\tau_{\text{m}}^{\text{failure}} = \left(1 - \frac{\chi}{\Delta\chi}\right)\tau_{\text{m}}^{\text{initial}} + \frac{\chi}{\Delta\chi}\tau_{\text{m}}^{\text{calc}}. \tag{8}$$

In this formulation, tensile failure occurs before shear failure if

$$\frac{\Delta\chi_{\text{tensile}}}{\chi_{\text{tensile}}} > \frac{\Delta\chi_{\text{shear}}}{\chi_{\text{shear}}}, \tag{9}$$

otherwise shear will be the first mode of failure. In other words, for a large stress change that exceeds both the tensile and shear failure criteria, the mode of first failure is that with the largest fractional change in failure proximity.

By application of these criteria to the distribution of elastic stress around faults, the distribution and style of brittle failure within the matrix can be determined.

2.3. Constitutive law for faults

Faults are represented as discrete finite surfaces in three-dimensions and their mechanical behaviour is specified according to boundary conditions on an elastic medium. In this way, we follow the well-known and relatively simple approach of describing faults as elastic dislocations (e.g. Chinnery, 1961; Rodgers, 1980; Pollard and Segall, 1987). One method is to specify the displacement discontinuities across the faults. However, this requires the a priori description of the slip distribution on each fault, which is often unknown and can lead to inconsistencies between fault-slip and the remote load stress. We choose to approximate faults as a weak frictionless interface by specifying zero in-plane shear traction and zero fault-normal displacement boundary conditions. By using in-plane traction boundary conditions, we specify a simple constitutive law for the faults.

Although faults are never truly frictionless, we contend the frictionless assumption remains meaningful in this context if the fault sustains a shear stress decrease of at least 90%. This is investigated explicitly as part of the sensitivity analysis presented later.

2.4. Link between remote stress and constitutive laws

The magnitudes of remote stress components are required to compute the elastic stress field. However, this is usually unknown and must be estimated by some means. The presence of faults indicates that stress reached the local shear failure envelope at the time of fault slip. Rock strength typically decreases with increasing length-scale as both the number and size of defects contained within the rock increases (Weibull, 1939). Therefore, it can be expected that the rock strength appropriate to fault formation is less than the rock strength appropriate to the formation of smaller scale secondary fractures. The rock strength governing fault formation depends on potentially many different mechanical layers over a length-scale comparable with that of the faults, whereas, rock strength on a length-scale less than that of the faults governs secondary failure potentially confined to single mechanical layers. Just as a change in failure proximity, $\Delta\chi$, can result from a change in stress, it can also result when the same stress state is compared with a different rock strength. Hence, we choose to represent the difference between rock strength appropriate to faulting and secondary fracturing with the quantity $\Delta\chi$.

The magnitude of remote mean stress, $\sigma_{\text{m}}^{\text{r}}$, and maximum shear stress, $\tau_{\text{m}}^{\text{r}}$, can both be determined according to the effective vertical stress at the time of deformation and the style of deformation. To cause fault slip, the remote stress must be located at the regional shear failure envelope. We assume one of the principal remote stresses to be vertical so that the vertical normal stress equals the weight of the overburden, and that the intermediate stress is equal to the mean stress. With these assumptions, Eq. (5) can be adapted to

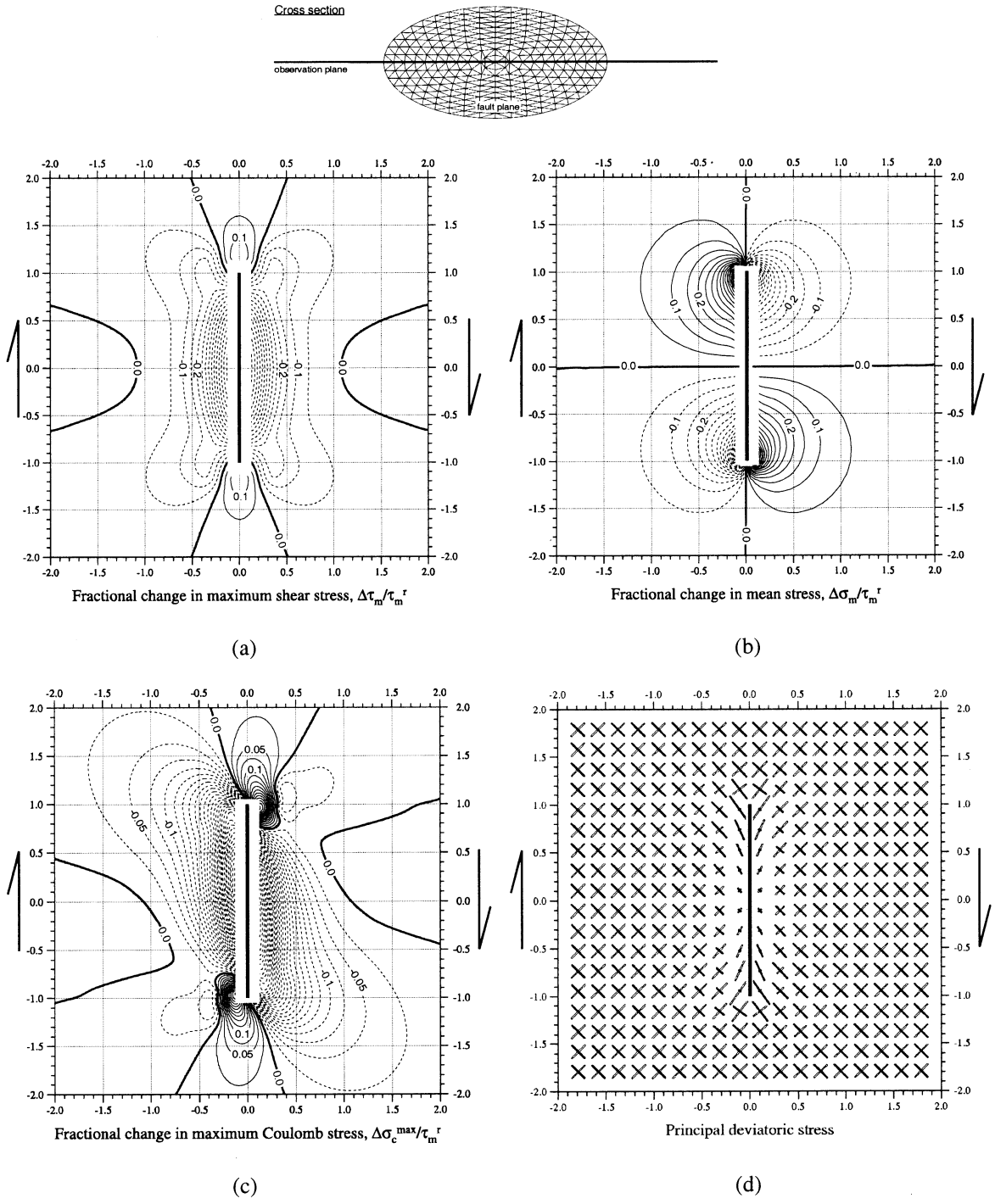

Fig. 3. The state of stress around an isolated right-lateral strike-slip fault. The fault is considered to be a planar frictionless surface with an elliptical tip line of aspect ratio 2 fault within a homogeneous, isotropic, linear elastic medium. Contours are shown of the fractional change in: (a) the maximum shear stress, $\tau_m = (\sigma_1 - \sigma_3)/2$, (b) the mean stress, $\sigma_m = (\sigma_1 + \sigma_3)/2$, and (c) the maximum coulomb stress, $\sigma_c^{max} = \tau_m - \mu\sigma_m$, where σ_1 and σ_3 are the most and least compressive principal stresses, respectively, and μ is the coefficient of internal friction taken here to be $\mu = 0.6$. In each case the change in stress is normalised with respect to the remote maximum shear stress τ_m^r. The most and least compressive principal deviatoric stresses, $\sigma_{1,3} - \sigma_m^r$, where σ_m^r is the remote mean stress, are indicated in (d). The orientation and magnitude of s_1 and s_3 are denoted by black and white bars, respectively. By convention compression is positive.

write the critical stress state as:

$$\sigma_m^r = \sigma_v' + \alpha\tau_m^r,$$

and

$$\tau_m^r = \frac{\sigma_v'\sin\phi + C\cos\phi + \Delta\chi}{1 - \alpha\sin\phi}, \tag{10}$$

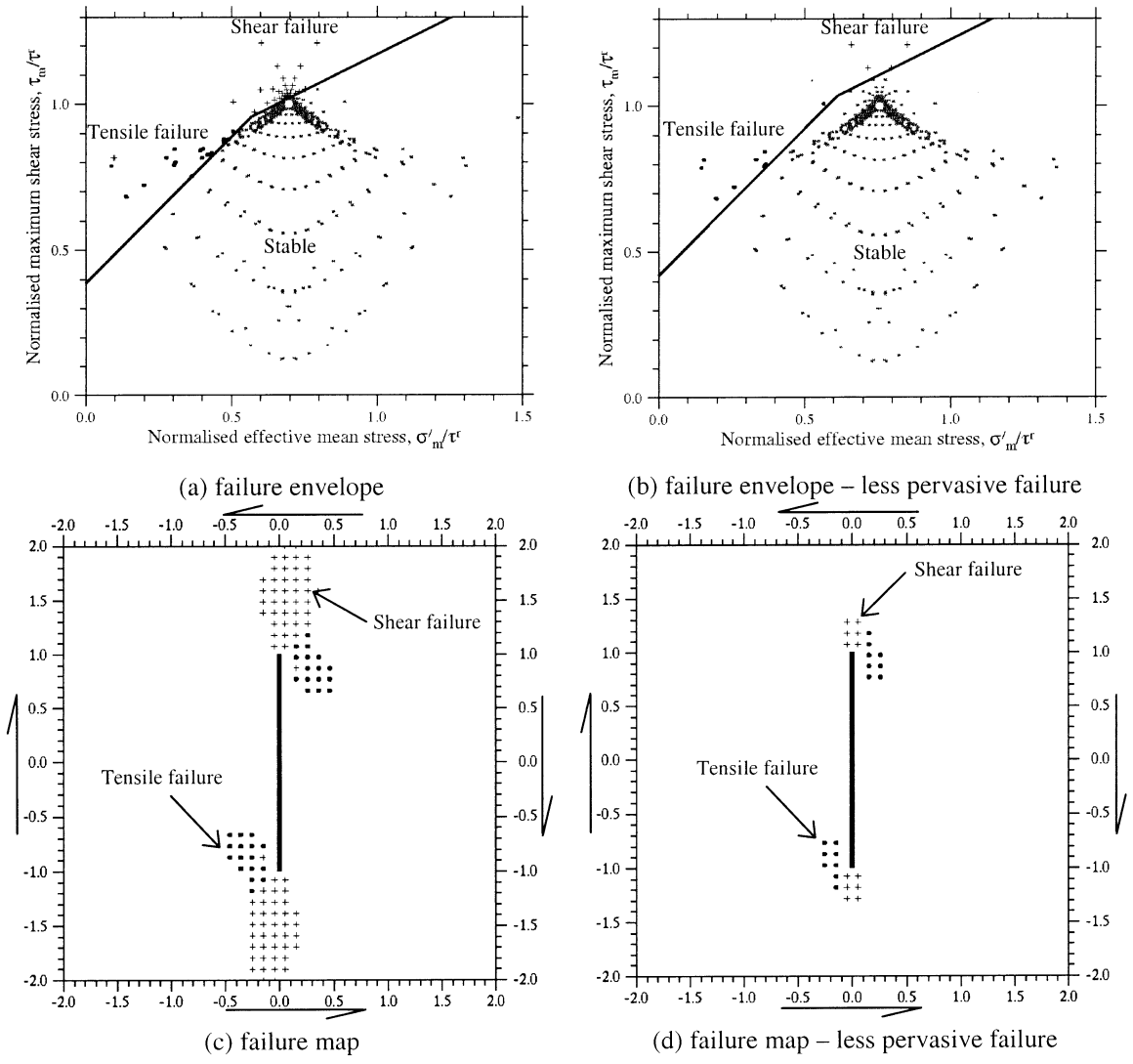

Fig. 4. Example of brittle failure states arising from the distribution of elastic stress around the isolated strike-slip fault shown in Fig. 3. The different stress states induced around the fault are shown in relation to the brittle failure envelope in (a and b) and by their location relative to the fault in (c and d). The initial stress before fault slip is denoted in (a and b) by the open circle. As a consequence of fault slip, the stress field is perturbed from its initial value and those points that cross the failure envelope correspond to either tensile or shear failure. Differences between the two examples illustrate the effect of changing the remote stress magnitude relative to the local rock strength. Note that the failure envelope is the same as that in Fig. 2 but appears different as it is plotted against different measures of stress.

where α equals $-1/2$, 0, 1/2 for normal, strike-slip and thrust fault environments, respectively, and ϕ and C are bulk material properties on a length-scale appropriate to secondary fracture formation. The effective vertical stress, $\sigma'_v = h\rho g - P_f$, where h is the thickness of the overburden at the time of deformation, ρ is the mean density of that overburden, g is the acceleration due gravity, and P_f is the pore fluid pressure. In this manner, the balance between remote stress and local rock strength is reconciled using the local constitutive law of the matrix and represented by the material parameter, $\Delta\chi$ and depth at the time of deformation.

2.5. Solution method

The equations of elasticity and stress balance were solved numerically for realistic fault geometries in three-dimensions subject to a remote stress field, but neglecting the effects of gravity. Solutions were obtained using *Poly3D* (Thomas, 1993), which is a three-dimensional boundary element code based on the linear elasticity theory and the displacement discontinuity method (Comninou and Dunders, 1975; Jeyakumaran et al., 1992). This code allows for triangular dislocations, which permit a much better representation of the geometry of many fractures than a code that relies on rectangular dislocations (e.g. Okada, 1985).

Many codes can calculate the elastic stress distribution associated with a fault or fault network given knowledge of the slip distribution across each fault. This stems from analytic solutions derived for this problem (e.g. Rongved

and Frasier, 1958; Steketee, 1958; Chinnery, 1961; Okada, 1985). However, this approach does not explicitly allow for the effect of mechanical interactions between faults, which can be significant. Within a fault network where the spacing between faults is less than the smallest fault dimension, these interactions are expected to dominate the overall distribution of stress (Willemse et al., 1996). Such mechanical interactions between closely spaced faults are calculated as a consistent part of the solutions because stress boundary conditions are used to represent the faults.

Previous applications of elastic faulting models to geological problems include fault interaction (e.g. Bürgmann et al., 1994; Willemse, 1997), fault growth (e.g. Segall and Pollard, 1980; Cowie and Scholz, 1992; Scholz et al., 1993; Cowie and Shipton, 1998), fault linkage (Aydin and Schultz, 1990; Crider and Pollard, 1998), and fault-related fracturing (e.g. Pollard and Segall, 1987; Martel and Boger, 1998)

3. Example application to brittle failure around an isolated fault

Fig. 3 illustrates the distribution of elastic stress calculated around an isolated elliptical strike-slip fault whose horizontal length is twice its vertical height. The post fault-slip stress fields are presented as fractional stress changes relative to the maximum remote shear stress, τ_m^r (for a fault at a depth of 1 km, τ_m^r is likely to be in the range 5–20 MPa).

The lateral distribution of maximum shear stress, represented in Fig. 3(a), shows, on average, a reduction in shear stress around the fault as a consequence of fault slip. However, shear stress does increase significantly ahead of the fault tips. The distribution of mean stress shown in Fig. 3(b) indicates a reduction across two quadrants associated with fault-parallel elongation of rocks that are displaced away from the tip line. Conversely, displacement of rocks towards the fault tips induces increased mean stress within the opposing quadrants. Reduction of fault-parallel shear stresses near the fault causes the orientation of principal stress to rotate locally towards either fault-parallel or fault-perpendicular directions as shown in Fig. 3(d). Such perturbations in the orientation of principal stress will be reflected in the orientation of any brittle fractures formed near the fault. The stress perturbations die off to small levels by a distance from the fault equal to the smallest fault dimension, in this case the fault height.

Fig. 4 shows the distribution of brittle failure associated with the elastic stress fields shown in Fig. 3. Two examples are shown, characterised by different ratios between the remote load and local rock strength. The difference is manifest in the different positions of the open circle in Fig. 4(a) and (b). In both examples, shear failure occurs ahead of the fault tips, and tensile failure just behind the fault tips within the quadrants of reduced mean stress. Reducing the remote stress magnitude relative to the local rock strength, $\Delta\chi$, reduces the extent of failure and ultimately restricts failure to rock directly adjacent to the tip line. In this example, the partitioning between tensile and shear failure is primarily determined by cohesive rock strength, C, which in Fig. 4 is $0.75\tau_m^r$. Pervasive tensile fracturing will occur when the remote mean effective compressive stress meets the following criterion:

$$\sigma_m \leq \frac{C(\cos\phi - 0.5) - \Delta\chi}{(1 - \sin\phi)} \tag{11}$$

4. Brittle failure around a small fault network at Nash Point

4.1. Geological setting

Nash Point is situated at the northern edge of the Bristol Channel Basin (longitude 3°33′ W, latitude 51°24′ N) as shown in Fig. 1. Along the coast, Triassic and Jurassic rocks are exposed, often along horizontal wave-cut platforms 100–150 m wide at low tide, providing opportunities to study large-scale fracture patterns. Exposures along the beach at Nash Point consist of inter-bedded Liassic shallow marine pale grey limestones and shales. Individual layers are rarely greater than 1 m thick, are laterally continuous for up to 2 km except where faulted, and dip consistently to the south at less than 5°.

The fracture patterns exposed at this location have been described and mapped in detail (Rawnsley et al., 1992; 1998; Petit et al., 2000) and examples of perturbed fracture trajectories around faults shown to be consistent with elastic stress trajectories observed within photo-elastic models. Fig. 1(a) shows an example where a geometrically simple fault network is associated with a complex pattern of tensile fractures. Based on regional geological knowledge (Chadwick, 1986; McLachlan, 1986; Brooks et al., 1988; Peacock and Sanderson, 1992), the faults are conjugate strike-slip faults related to Late Cretaceous to early Tertiary Alpine shortening. To the east of Nash Point, a major 140° striking dextral strike-slip fault zone extends for over 5 km (St. Donats fault). Striations on this fault were previously measured and analysed using the Etchecopar inverse method to yield an azimuth of maximum horizontal contraction between 170 and 180° (Rives, pers. commun.).

4.2. Model results

The ability of the methodology described above to predict fault-related fractures at Nash Point can be assessed in two ways. First, the calculated principal stress magnitudes should be consistent with tensile rather than shear failure. Second, the calculated orientation of principal stresses should reproduce the observed fracture trajectories.

The three-dimensional geometry of faults at the Nash Point outcrop used for elastic stress calculations is shown

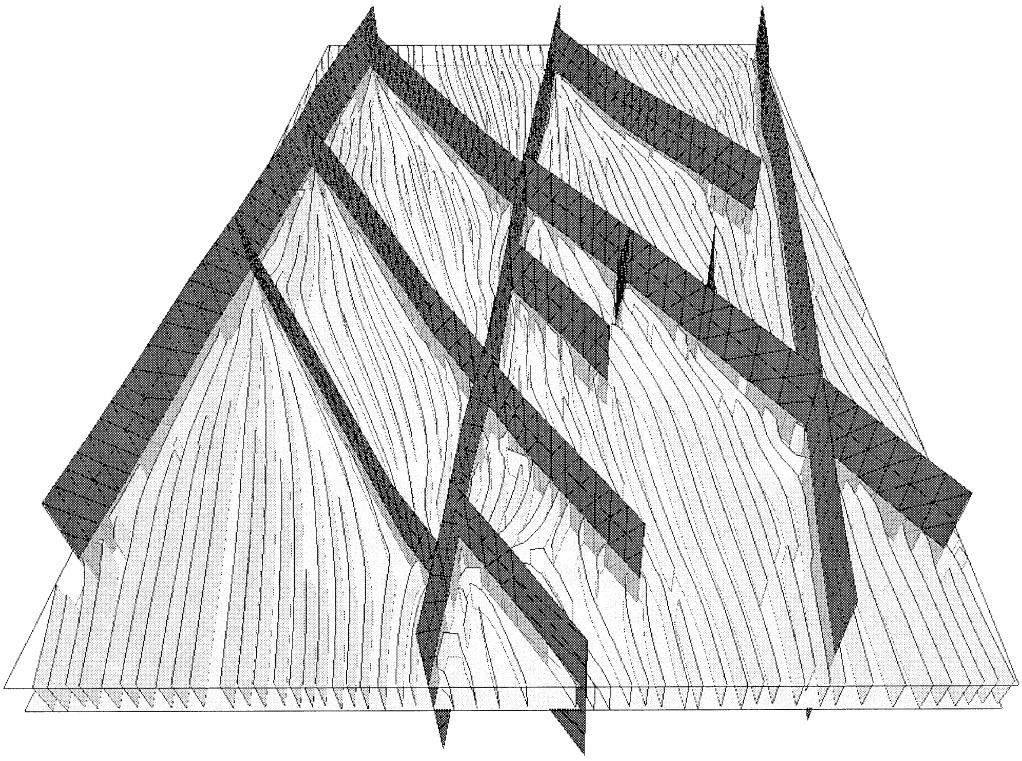

Fig. 5. A perspective view, looking north and down onto one of the three-dimensional fault and fracture models calculated for the Nash Point outcrop. Each fault is represented by a series of triangular elements of mean horizontal edge length 2 m. Within the single matrix layer shown, tensile fracture growth has been simulated according to the field of elastic stress calculated around the faults. Note that this layer is shown with vertical exaggeration for the purposes of clarity.

in Fig. 5 based on the fault map produced by Petit et al. (2001). We assume the faults are vertical, rectilinear, and of constant height. The primary model described here has a fault height of 40 m, which is equal to twice the mean spacing of the north-west striking fault set.

The remote stress responsible for this strike-slip fault geometry is considered to be oriented with the maximum compressive principal stress along an azimuth of 170°. Elastic properties of the matrix are represented with a Young's modulus of 10 GPa, and a Poisson's ratio of 0.25. The faults were represented using triangles with a the mean horizontal edge length of 2 m, hence fault slip distributions were resolved on this length-scale. The stress field around the faults was evaluated on a horizontal regular grid of points with a 1 m spacing. This grid was located at the mean depth of the fault network. All the models considered have this same resolution.

4.2.1. Fracture initiation

Fig. 6(a) and (b) shows the distribution of brittle failure resulting from the calculated elastic stress field. The magnitude of calculated stress is proportional to the remote shear stress, τ_m^r, therefore in Fig. 6 we normalise the calculated stress field by this factor. In this example the difference between regional and local rock strength is almost zero ($\Delta\chi = 0.05\tau_m^r$) and the cohesion is $C = 0.4\tau_m^r$. This results in limited tensile and shear failure initially within the matrix (4 and 5%, respectively) close to fault tips and intersections. Whilst it is true fractures initiating within these regions may propagate sub-critically into regions where fractures do not initiate, they would not propagate far into those regions because the stress states there are generally located well away from the failure envelope. Even in the event that cohesion takes the maximum value permitted by Eq. (11), just 10% of the region underwent tensile failure and 2% shear failure. Therefore, the assumption of elasticity for computing the fault-related stress field is reasonably robust since just 12% of the rock considered exceeded its elastic limit as a consequence of faulting.

In order to explain the pervasive opening-mode fracture pattern related to faulting at Nash Point, an additional and essentially isotropic stress change is required. An isotropic stress change of $0.8\tau_m^r$, as shown in Fig. 6(c) and (d), produces almost complete tensile failure of the rock (85%) with shear failure still limited to areas around fault tips and intersections (7%). Such an isotropic stress change after faulting can, for instance, arise from an increase in pore fluid pressure, erosion of the overburden, a decrease in rock temperature, or some form of diagenetic change. The presence of tensile residual stress, for instance due to bonding between layers with different thermo-mechanical rock properties (Holzhauzen and Johnson, 1979), may also contribute to the generation of tensile stress.

At Nash Point, significant erosion has certainly occurred.

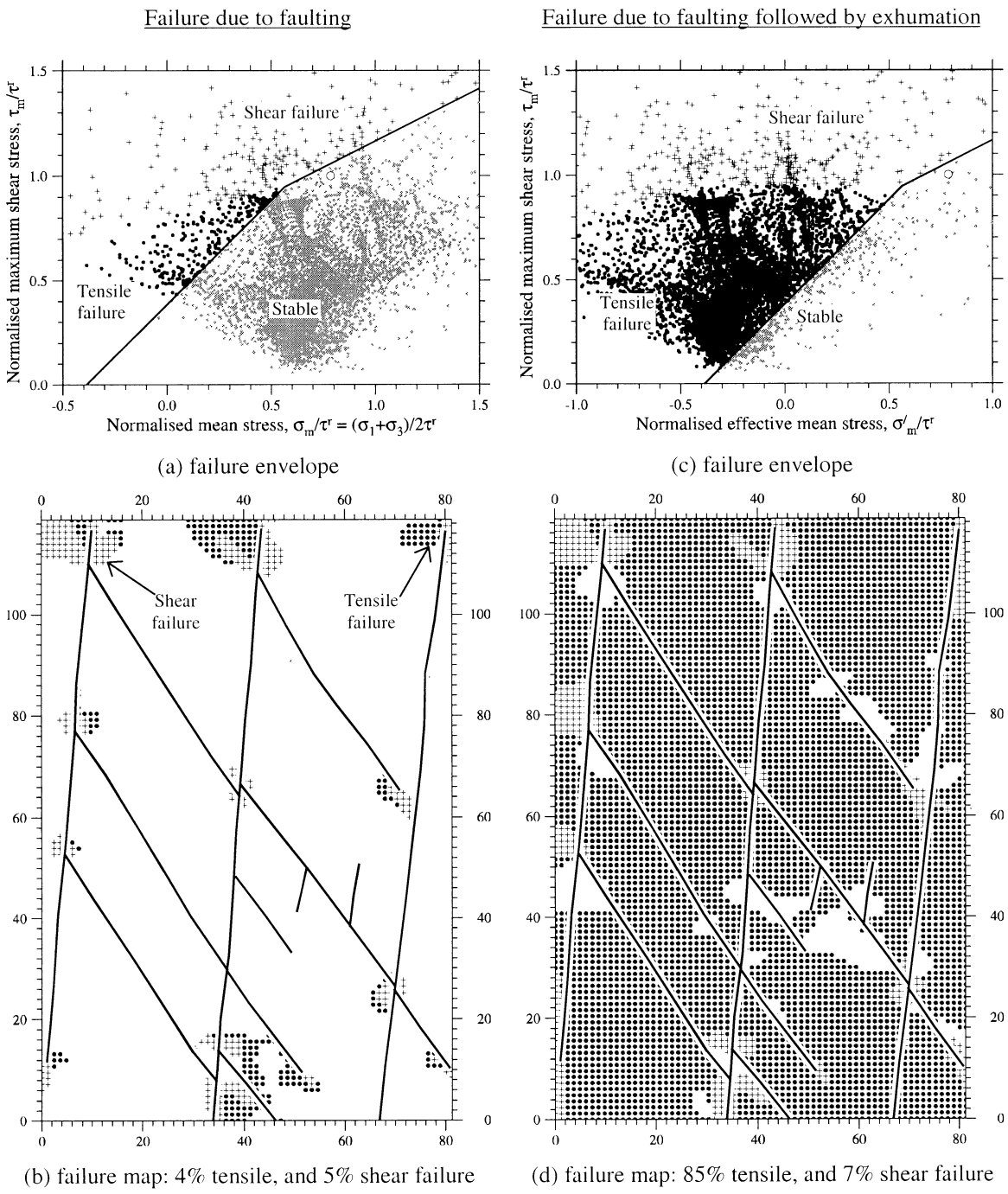

Fig. 6. Brittle failure associated with an elastic stress field calculated for the Nash Point fault network. Failure resulting from fault slip alone is shown in (a) and (b). This demonstrates that fault slip is not the mechanism that triggered pervasive tensile fracturing of the rock at Nash Point. However, the subsequent action of an isotropic stress change due to erosion, or a change in temperature or pore fluid pressure in the range 0.8–1.0τ^r_m can produce 80–90% tensile failure in this example.

However, this can only explain the origin of opening-mode fractures if the amount of erosion exceeds a certain limit. Too little erosion means the faults would need to form at such shallow depths that cohesion would be sufficiently great to allow pervasive tensile failure prior to fault formation. Therefore the fault would be related to tensile fracturing rather than vice-versa as observed. This lower limit on erosion follows directly from Eq. (11):

$$\sigma'_v \geq \frac{C(\cos\phi - 0.5) - \Delta\chi}{(1 - \sin\phi)} \tag{12}$$

where σ'_v is the vertical stress at the time of strike-slip faulting. Evaluating Eq. (12) for the rock properties used in Fig. 6 requires effective vertical stresses at the time of

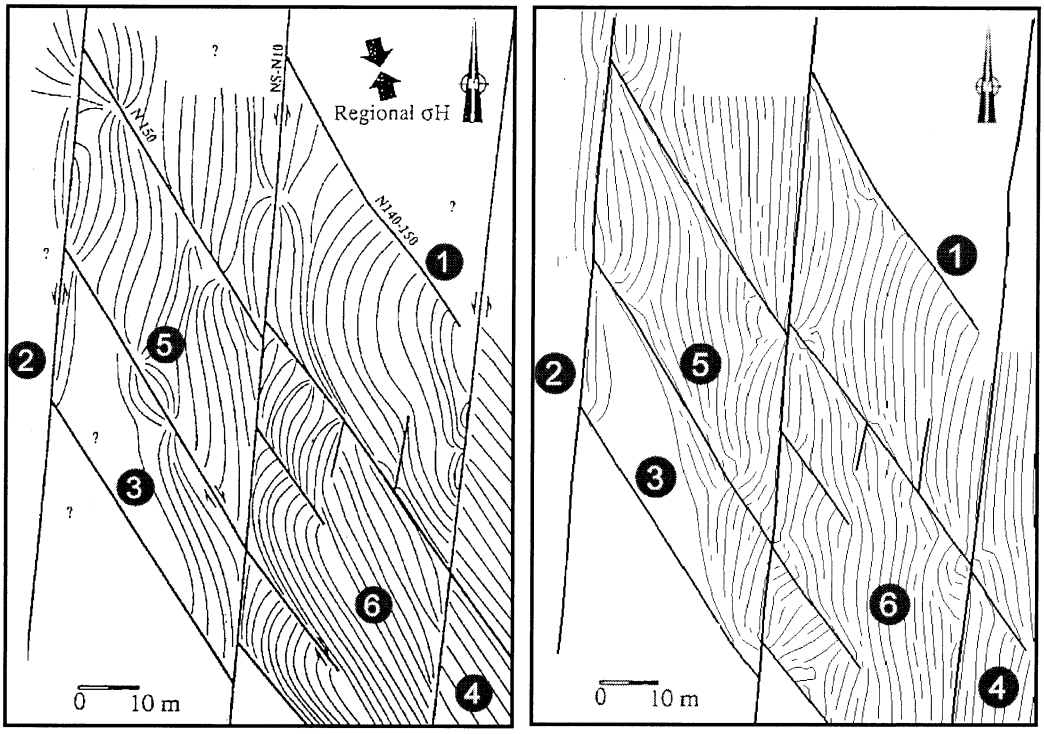

(a) observed fracture pattern (b) calculated fracture pattern

Fig. 7. The observed and calculated patterns of fracturing produced by stress perturbations around faults near Nash Point, Bristol Channel, UK. Faults are denoted by thick straight lines, and fractures by thin curved lines. Fig. (a) is taken from Petit et al. (2001). Note that the numbered labels refer to numbered items within the text.

faulting greater than 7 MPa, which for hydrostatic pore fluid pressures corresponds to a depth of at least 400 m.

4.2.2. Fracture propagation

Once initiated, tensile fractures open in the direction of the least compressive stress and propagate perpendicular to this direction. In the case of Nash Point, fractures propagated within individual layers and the observed fracture traces are essentially the result of horizontal propagation. Fig. 7 shows a comparison between the observed and calculated fracture trajectories. The calculated fracture pattern was generated by simulating fracture growth. Fractures were initiated at points selected at random within areas of tensile failure, propagated perpendicular to the direction of minimum horizontal compressive stress. Fractures were then terminated either against faults, at the edge of failed regions, or at a specified distance from other fractures. The latter criterion is chosen to represent the effect of stress release around fractures zones in which other fractures cannot propagate. The half-width of this forbidden zone is taken to be equal to the smallest dimension of the fracture to reflect the width of significant stress release according to the analytic solution for a mode I crack within an infinite elastic medium (Pollard and Segall, 1987). This encourages the development of a fracture set with an approximately regular spacing equal to the bed thickness, which is a common feature of fractured outcrops (Price, 1966).The calculated fracture pattern reproduces the observed fracture pattern on length-scales above the model discretisation, i.e. 2 m. Where fractures are observed to have grown parallel or perpendicular to fault segments this is reproduced in the calculated fracture map. For example, at the location labelled number 1 in Fig. 7, both observed and calculated fractures grow away from this fault at right angles and curve back towards the direction of regional contraction, 170–180°, over a distance of ca. 20–30 m. At location number 2, both observed and calculated fractures are oriented at ca. 30° to the trend of regional fractures, yet parallel to the adjacent fault segment. Furthermore, where fractures grew between adjacent faults that are expected to interact mechanically the direction of calculated fractures is comparable with that observed. For instance, at location 3 both observed and calculated fractures grew diagonally across the fault block within 10° of the direction of regional contraction.

On the outside edges of faults situated near the boundaries of the model, unseen faults or fault segments just beyond the limits of the map will exert an effect that is not calculated, such as at location 4. Here, the calculated fractures run parallel to the north-north-east striking fault rather than, as observed, parallel to the north-west striking fault. Extending the north-west striking fault to the south-east we are able to reconcile this difference. This kind of edge effect only affects regions in the model that are not surrounded on all sides by faults.

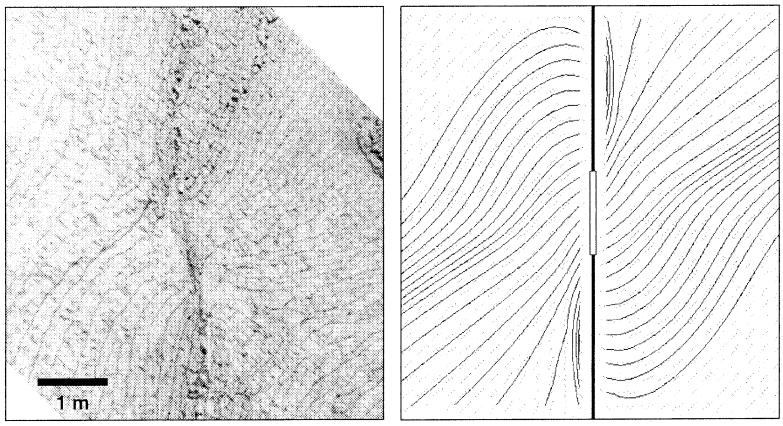

Fig. 8. Comparison between observed and calculated tensile fracture trajectories associated with a small fault kink or asperity. The calculated pattern is based on the linear elastic model of stress around a fault with the asperity represented as a segment with no fault slip. The calculation reproduces the observed pattern in all but the top left corner where the effects of another fault kink interfere.

Unobserved faults have the potential to cause errors within the area of interest, and the larger the unobserved fault the larger the error in the calculated stress field. A possible example is shown at location 6 where the observed fracture pattern strikes parallel to the nearby north-west trending fault. In error, the calculated fractures cut across this region in a northerly direction, some 40–50° away from the observed direction. In terms of lateral extent, this is the largest mismatch between the observed and calculated fracture distributions. The calculated fracture pattern can be made more consistent with that observed by allowing the nearby fault to extend further to the south-east either above or below the plane of the outcrop. Such a geometry is quite plausible as faults typically have an elliptical tip line.

Unobserved small-scale bends and kinks on a fault plane can act as local stress concentrators that cause fractures to radiate out in many directions. These small-scale features do not appear in the calculated fracture pattern due to the 2 m grid node spacing in the calculated fault slip distribution. For example, the fracture pattern observed at location 5 exhibits sprays of fractures originating from two distinct points on the north-west trending fault trace. In contrast, the calculated fractures simply strike parallel to the fault. Simple linear-elastic stress calculations for a fault plane containing a small segment that remained stuck whilst the rest of the fault slipped are able to explain this kind of fracture concentration around a point (see Fig. 8).

Differences between the observed and calculated fracture patterns are restricted to features on length-scales smaller than those on which the faults are represented. Errors in the three-dimensional fault geometry, which was assumed to be as simple as possible, appear to be primarily responsible for these small-scale differences.

5. Sensitivity analysis

The orientation and magnitude of elastic stresses and hence the initiation and orientation of opening-mode fractures around the fault network at Nash Point will depend on: (i) fault geometry, (ii) remote stress, (iii) elastic properties, and (iv) fault friction according to the mechanical model so far discussed. The aim of the following analysis is to demonstrate how sensitive the calculated trajectory of fractures shown in Fig. 7(b) is to changes in these model parameters.

The sensitivity of a fracture prediction to model parameters has been analysed according to 34 independent stress and fracture calculations of the Nash Point outcrop. These calculations were separated into groups and, within each group, just one parameter was varied in order to assess its impact on the fracture prediction. Unless stated otherwise, model parameters are as previously described.

5.1. The role of fault heights

Fault dimensions exert a primary influence on the predicted fracture pattern, and are responsible for the wide range of fracture patterns. Fig. 9 shows results for fault heights of various fractions and multiples of the characteristic fault spacing, d, which is taken to be 20 m. Fault heights that are small compared with fault lengths or fault block widths (e.g. Fig. 9(b) and (c)), exhibit only tiny perturbations away from the regional trend of fracturing. These are all restricted to small regions close to the faults and do not extend across any significant fraction of the fault blocks. Further reductions in fault height only act to further localise the perturbed fractures around the faults. For much larger fault heights (e.g. Fig. 9(h) and (i)) the fracture pattern is vastly more complex with every fault block completely invaded by heterogeneous fracturing. Fig. 9(h) and (i) are already similar to each other and a further increase in fault height does not cause any noticeable changes from these calculated fracture patterns. The height of faults at Nash Point is not directly known. An inspection of the map and model results suggests that a fault height of 40 m (Fig. 9(f)) yields the best match between the model and the observations. However, a 50% change in fault height still gives

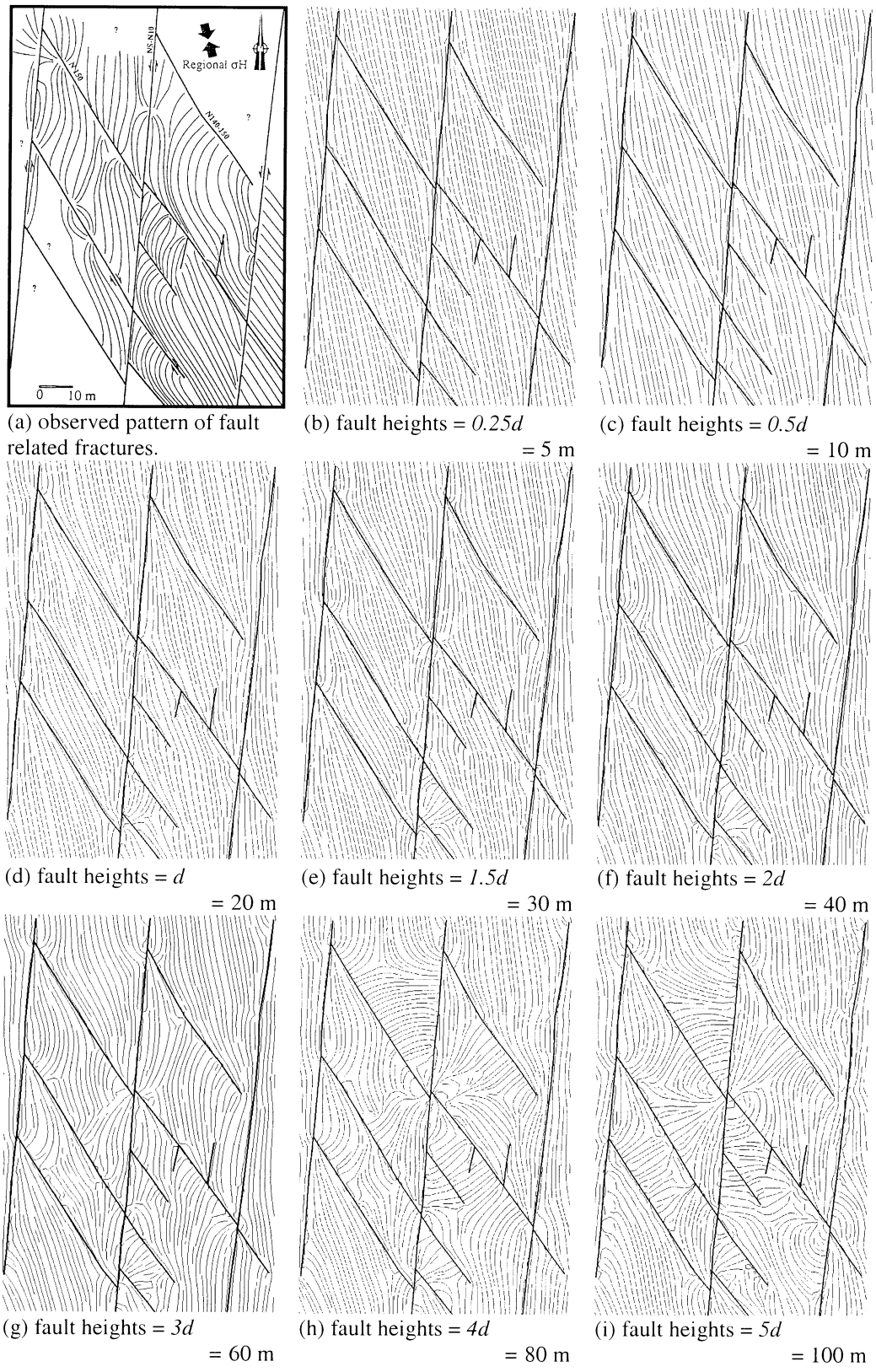

Fig. 9. The role of fault height versus fault spacing, *d*, in determining the pattern of fracturing. Fault separation, *d*, is taken to be 20 m, which represents the mean width of the fault blocks seen in this outcrop.

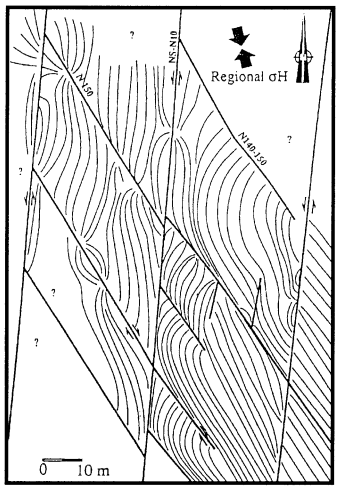

(a) observed pattern of fault related fractures.

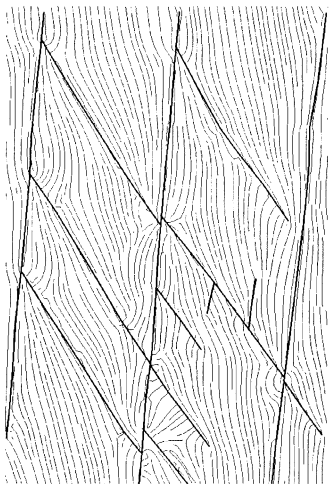

(b) distance to the top of the faults = $h/2$.

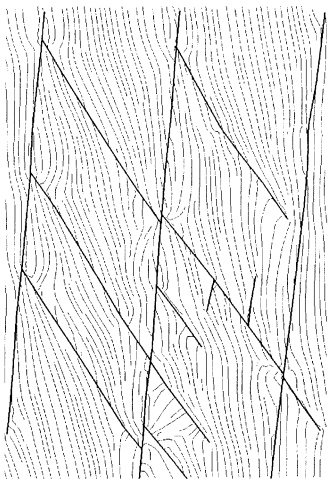

(c) distance to the top of the faults = $3h/8$.

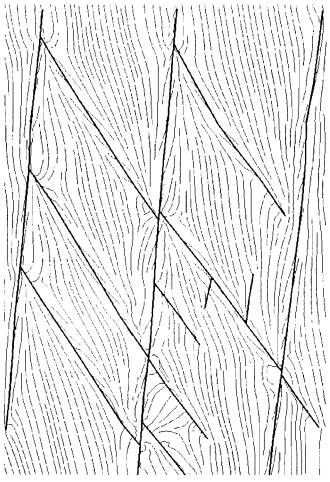

(d) distance to the top of the faults = $h/4$.

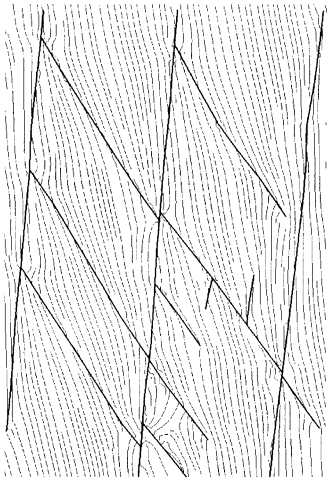

(e) distance to the top of the faults = $h/8$.

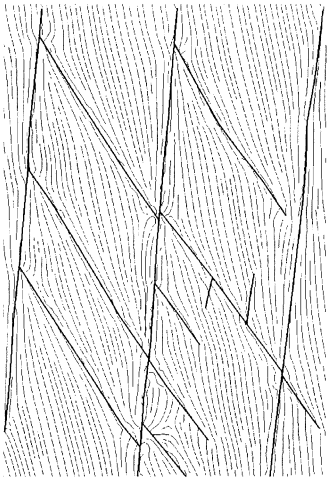

(f) distance to the top of the faults = $3h/32$.

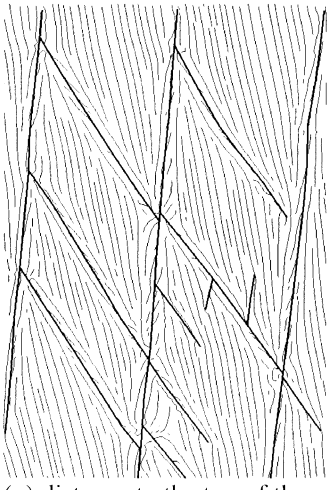

(g) distance to the top of the faults = $2h/32$.

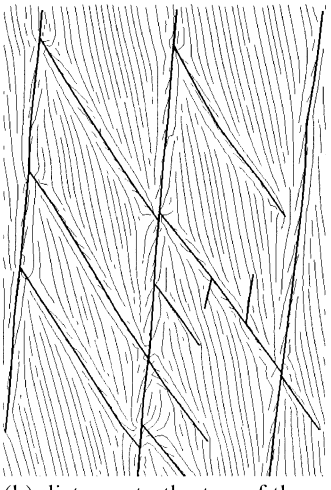

(h) distance to the top of the faults = $h/32$.

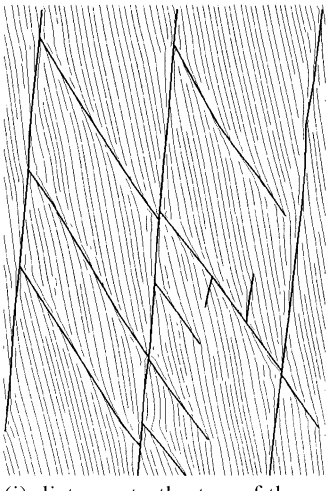

(i) distance to the top of the faults = 0.

Fig. 10. The role of distance from the plane of the outcrop to either the top or bottom fault tips in determining fracture distribution. The fracture distribution calculated at all levels corresponding to the middle 80% portion of the faults exhibit no significant changes. Only when the unseen top or bottom fault tips are less than ca. 10% of the fault height, h, away from the outcrop do significant changes in the calculated fracture pattern occur.

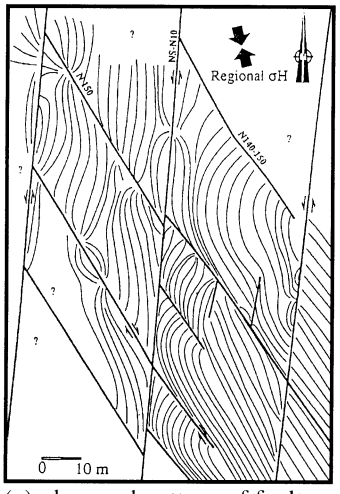

(a) observed pattern of fault related fractures.

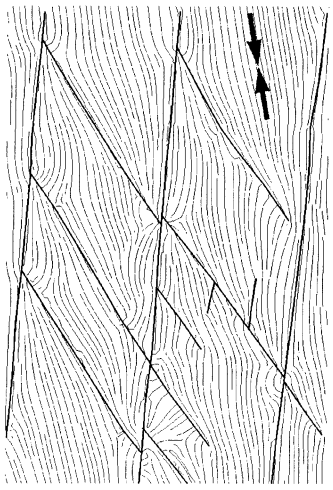

(b) uniaxial contraction oriented 170°.

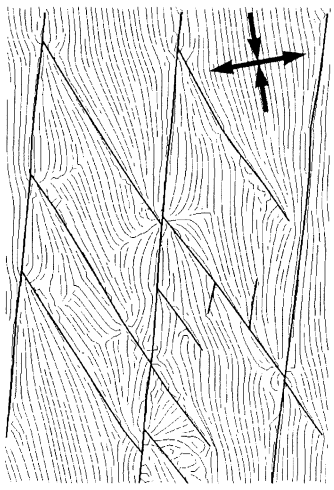

(c) pure shear, with contraction oriented 170°.

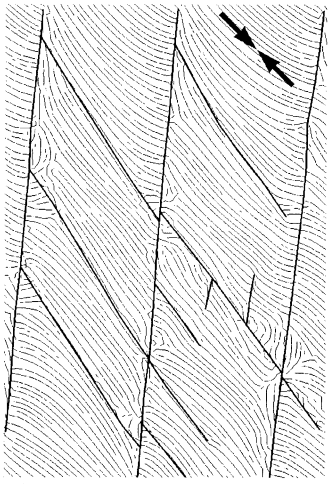

(d) uniaxial contraction oriented 140°.

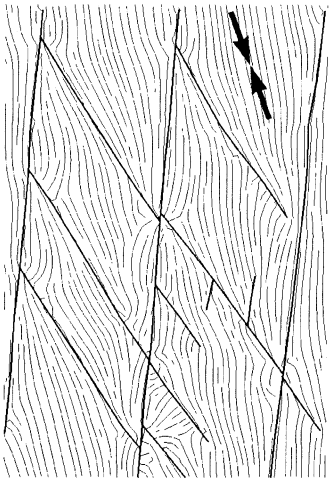

(e) uniaxial contraction oriented 160°.

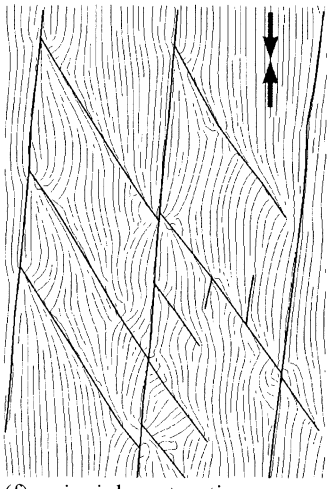

(f) uniaxial contraction oriented 180°.

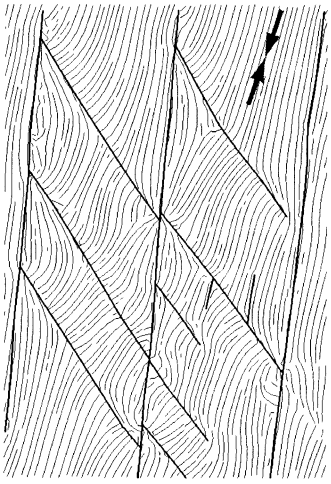

(g) uniaxial contraction oriented 200°.

Fig. 11. The role of remote stress in determining the pattern of fracturing. Calculated stress trajectories and hence fracture paths depend only on the orientation of remote principal stresses and not their absolute or relative magnitudes; e.g. (b) and (c). Significant differences only arise when the direction of contraction differs from the true value by at least 20°; e.g. (d) and (g).

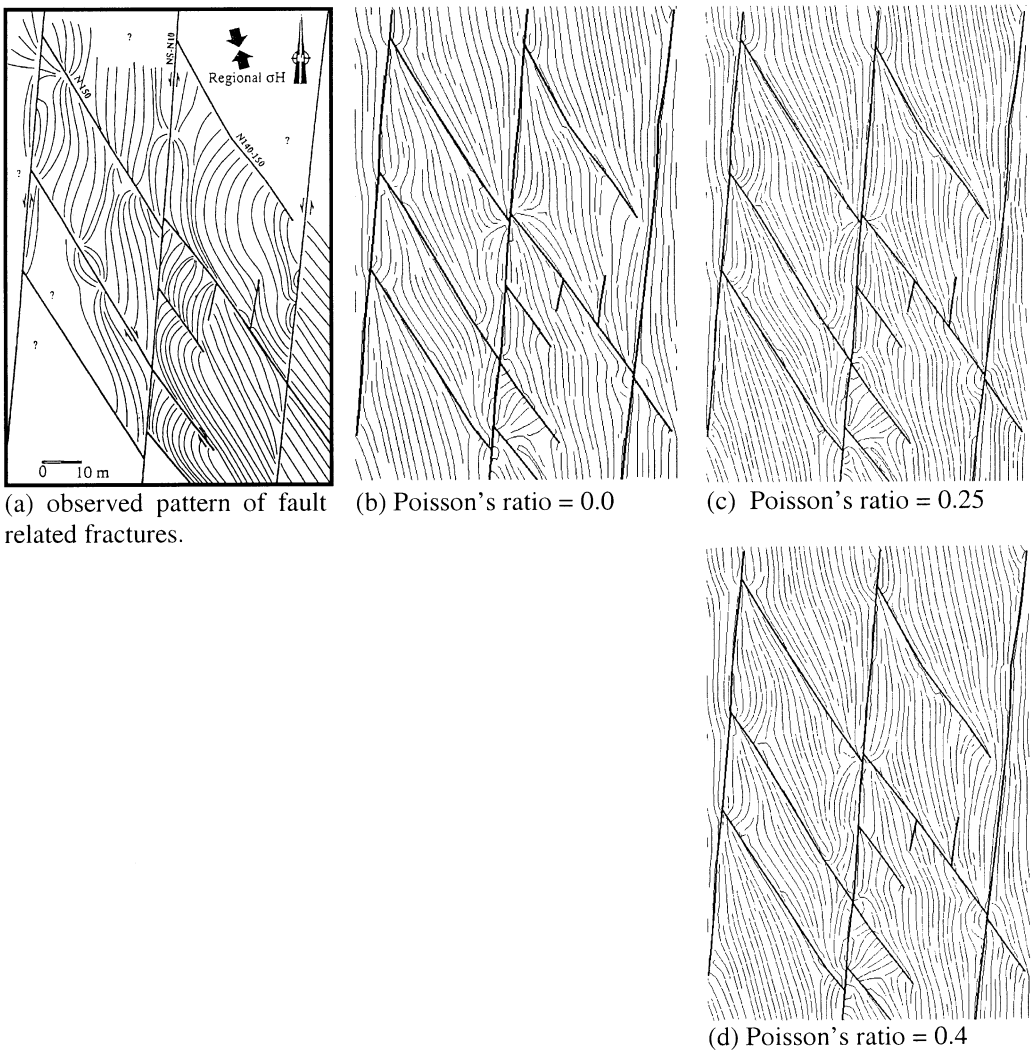

(a) observed pattern of fault related fractures.

(b) Poisson's ratio = 0.0

(c) Poisson's ratio = 0.25

(d) Poisson's ratio = 0.4

Fig. 12. The role of Poisson's ratio in determining the pattern of fracturing. An increase in Poisson's ratio causes stress perturbations to diffuse further from the faults leading to greater interactions between the fractures and the faults and between the faults themselves. Within the range expected values for rocks (0.1–0.4) calculated fracture distribution are not sensitive to uncertainties in Poisson's ratio, c.f. (b)–(d).

a reasonable match (c.f. Fig. 9(e) and (g)). In these cases, the fault height is comparable with the mean fault spacing, analogous to the ratio between the height and spacing of opening-mode fractures surrounding the faults where spacing comparable with the 1 m bed thickness.

These results demonstrate that the calculated elastic stress field is sensitive to fault height if it is the smallest fault dimension. In this case, uncertainties of 50% can be tolerated without introducing significant errors in the calculated fracture pattern.

5.2. The effect of proximity to top or bottom fault tips

The state of stress around a fault tip changes rapidly with position and can lead to significant changes in fracture orientation and intensity over length-scales considerably smaller than the size of the fault. The effect of proximity to the unseen top or bottom tip lines of the faults at Nash Point is assessed in Fig. 10. Due to symmetry, the effects of proximity to either top or bottom tip lines are identical in this case. As the faults are observed to intersect the fractured layer in outcrop, we only consider these cases in the model. In the vicinity of faults but away from their top and bottom tip lines (e.g. Fig. 10(b)–(d)), fractures orient themselves either parallel or perpendicular to fault planes. Once either the top or the bottom tip lines are within approximately one eighth of a fault height of the fractured layer (Fig. 10(e)–(i)), the calculated fracture orientations show very little perturbation away from the direction of regional contraction. However, near these tip lines shear stresses are increased relative to the remote shear stress. This can result in arrays of finely spaced en-échelon shear fractures running along the fault tip line (Martel and Boger, 1998).

The pattern of fracturing observed at Nash Point is best explained by a set of faults whose top and bottom tip lines lie at least 10 m out of the plane of the outcrop (i.e. more

than a quarter of a fault height away). It is interesting to note that apparently the Nash Point outcrop is such a striking example of fault-related fracturing largely because the exposed fractured beds currently lie close to the vertical centre of the faults. Further erosion at this site is likely to reveal progressively less heterogeneous opening-mode fracture patterns as indicated in Fig. 10(e)–(i).

5.3. The role of remote stress

Remote shear stress governs the way a given fault network accommodates strain and hence perturbs the local stress field. Any isotropic component to the remote stress, e.g. the mean confining pressure, will not cause slip on frictionless faults and hence will not introduce a fault-related perturbation in our model of the local stress field. Therefore, the calculated perturbed stress field is only sensitive to those components of the remote stress state that resolve shear stress on the faults. The assumed vertical faults at Nash Point constitute a special case in which the vertical principal stress does not resolve any shear stress on any part of the fault network. As a consequence, horizontal trajectories along which fractures would grow are only sensitive to the orientation of the most compressive horizontal stress. Fig. 11(b) and (c) show remote loads corresponding to uniaxial contraction in (b) and pure shear in (c), both with the same orientation of most compressive horizontal stress. There are no differences in the computed trajectory of fractures whatsoever. Small differences are visible between the two fracture patterns of (b) and (c) but these only occur because of the random sequence in which fracture growth was simulated.

Fig. 11(d)–(g) illustrates the effect of small changes in the direction of remote compression. Within 10° of the expected direction of compression, little difference can be observed between the calculated fracture trajectories (Fig. 11(e) and (f)). Variations of greater than 10° in the direction of remote compression produce considerably different fracture trajectories, which bear little relationship to the observed pattern of fracturing in Fig. 11(a). The best-fit fracture prediction, as judged by inspection, is shown in Fig. 7(b) and also corresponds to Fig. 11(f).

5.4. Sensitivity to elastic material constants

Describing the elastic properties of a rock using Young's modulus, E, and Poisson's ratio, ν, has the desirable effect of separating the effects of elasticity properties into two separate features of the elastic stress field around the faults. Young's modulus governs the magnitude of elastic stresses resulting from a given remote strain, and hence the calculated stresses are independent of E when remote stress boundary conditions are applied. In contrast, variation in Poisson's ratio, ν, affects the length-scale over which stresses are perturbed by the faults. Increases in Poisson's ratios result in perturbed stresses extending to greater distances from the faults. This leads to greater mechanical interaction between neighbouring faults (e.g. Willemse, 1997).

Fig. 12 illustrates the effect of Poisson's ratio on the fracture system at the Nash Point. Within the range of allowable limits for elastic materials ($0\nu0.5$) there is very little discernible difference between the different fracture patterns. Poisson's ratio is known to vary within sedimentary rocks, and in general decreases with depth because of crack closure (O'Connel and Budiansky, 1977). However, errors resulting from uncertainty in Poisson's ratio are negligible compared with those relating to fault geometry.

5.5. Influence of fault friction

Finding fault boundary conditions to correctly represent brittle failure is problematic. The simplest assumption is that fault planes are uniformly and perfectly weak, and so essentially frictionless. In this state, a fault would represent a surface free of shear traction as previously described. This assumption means that principal stresses adjacent to faults must be oriented either parallel or perpendicular to the fault planes. Such a perturbation in fracture trajectories is clearly observed near faults at Nash Point.

The effect of fault friction is to leave a residual in-plane shear traction on fault surfaces after fault slip. These tractions would cause stress and fracture trajectories adjacent to the faults to run obliquely to the fault surfaces. As the fault network is small, any variation in fault friction with depth can be neglected. The Nash Point faults all subtend essentially the same angle to the remote stress and so normal and shear tractions acting on the fault surfaces prior to fault slip will be essentially uniform, neglecting effects due to gravity. As such, a uniform coefficient of friction will result in an apparent constant, but incomplete, shear stress drop on all faults. Therefore, we can readily understand how the Nash Point fracture pattern would appear under conditions of constant fault friction.

Since the elasticity equations are linear, the principle of superposition holds. For instance, this means that a 50% stress drop on all faults can be judged on the basis of two stress calculations, one for a 100% stress drop, and the other for a 0% stress drop. These two solutions are both known — the former was previously calculated (e.g. Fig. 7(b)), and the latter is simply equal to the remote state of stress. Hence, stresses corresponding to a 50% stress drop would at any point be equal to the mean value of the 100 and 0% solutions at that point. Any fractional stress drop can be similarly represented by an appropriate linear combination of these two solutions. Consequently, faults retaining increasingly more shear stress give rise to fractures perturbed by progressively smaller angles from the direction of regional fracturing and increasingly oblique to the fault planes. Hence the presence of fault friction would render the calculated fracture pattern less consistent with the pattern observed at Nash Point. For example, a 50% shear stress

drop on the faults would correspond to a maximum stress rotation of just 15° rather than the ca. 30° observed.

Descriptions of faults according to a constant fractional stress drop leads to extremely large gradients in fault slip near fault tips. This is not an observed property of geological faults (Cowie and Shipton, 1998). Nonetheless, this discrepancy only produces localised errors in the stress field around the fault tips compared with modified elastic models that produce finite fault tip displacement gradients (Martel, 1997; Willemse and Pollard, 1998). Therefore, the inter-fault regions of the calculated stress fields for Nash Point would be little affected by modifying the fault tip displacement gradients.

6. Conclusions

The pattern of opening-mode fractures observed at the Nash Point outcrop is related to, but more complex than, the pattern of larger strike-slip faults. These opening-mode fracture trajectories provide a record of the local orientation of maximum horizontal compressive stress at the time of fracture. The observed fracture pattern can be explained to first order by the elastic stress field developed around perfectly weak faults subject to a remote load. Elastic stress fields were calculated on this principle using the observed fault geometry, and kinematic evidence for the orientation of remote stresses at the time of faulting. Simulation of brittle failure and opening-mode fracture growth within the elastic stress field produced a fracture pattern very similar to that observed.

Although the opening-mode fracture pattern is related to faulting it is not primarily caused by faulting. The calculated magnitude of elastic stresses within the outcrop is sufficient to form only limited fault-related tensile and shear failure close to fault intersections and nowhere else. A pervasive fault-related pattern of opening-mode fractures therefore requires a subsequent and additional load to that imposed by faulting whilst the faults themselves remain essentially frictionless. The simplest and most effective additional load would produce an effectively isotropic reduction in compressive stress. Such loads may be internal to the outcrop, such as an increase in pore fluid pressure, a decrease in temperature, a diagenetic phase change, or even some combination of these effects. However, erosion of the overburden will also result in a similar effect. Considering erosion alone, faulting at a depth of at least 400 m below the present-day surface would yield pervasive faulted-related tensile failure. Allowing for any overpressure or temperature reduction generated by erosion would decrease the required depth of faulting.

The model is independent of time in all but one aspect. We assumed that just one fracture propagated at a time. This is reasonable if the rate of fracture initiation remains less than the rate of fracture termination. In this situation fractures grow to lengths comparable with the dimensions of fault bound blocks as observed at Nash Point. However, if the converse became true and many fractures propagated simultaneously, the number of fractures terminating against each other would become significant. In this situation ultimate fracture lengths would be significantly less than those observed. The rate of fracture initiation is governed by the rate of change of rock stress relative to strength. As such, the observed fracture lengths are consistent with a rate change of stress or strength that is small compared with the rate of fracture formation. This is consistent with the notion that fractures formed in response to a body force such as exhumation rather than fault slip.

While fault slip in response to a remote load is not considered to cause the majority of observed tensile fracturing, it does control the pattern of curve trajectories that fractures follow once initiated. Close to the faults this occurs because the local direction of principal stress is rotated from the regional trend to become either fault-parallel or fault–perpendicular as a consequence of complete shear stress release on the faults. This effect decreases with distance from the fault but extends out to a distance approximately equal to the smallest fault dimension. At Nash Point this smallest dimension is fault height. The observed fracture pattern is consistent with fault heights of 30–60 m.

Irregularities in fault geometry lead to stress concentrations and radial distributions of fractures stemming from the fault. These small-scale features can be calculated if the irregularity can be mapped out on the fault plane. In practice, the resolution of the calculated fracture pattern corresponds to the resolution at which the geometry of faults is measured.

The computed fracture trajectories are judged by inspection to best match those observed if the direction of the greatest remote horizontal compressive stress is oriented with azimuth $180 \pm 10°$. This is consistent with an independent measurement of 170–180° derived from nearby kinematic markers (Rives, pers. commun.). In contrast, the calculated fracture pattern is independent of Young's modulus, and essentially independent of Poisson's ratio. Variation of Poisson's ratio within the allowable limits (0–0.5) does not lead to any significant difference between the observed and calculated fracture patterns.

In summary the complex pattern of fracturing around faults at Nash Point, Bristol Channel, UK has been successfully explained and reproduced by the elastic-brittle model described. This result provides evidence to support the hypothesis that linear elasticity can be used to calculate local stress and strain increments around geological fault systems. This in turn lends confidence in the ability to predict fault-related fracture systems, in the subsurface, where they have a large economic impact.

Acknowledgements

Dave Pollard and Atilla Aydin, Stanford University are

thanked for access to *Poly3D*. This paper benefited greatly from careful reviews by Steve Martel and Patience Cowie.

References

Aydin, A., Schultz, R.A., 1990. Effect of mechanical interaction on the development of strike-slip faults with echelon patterns. J. Struct. Geol. 12, 123–129.

Bourne, S.J., Rijkels, A., Stephenson, B.J., Willemse, E.J.M., 2000. Predictive modelling of naturally fractured reservoirs using geomechanics and flow simulation. GeoArabia 6 (1), 87–102.

Brooks, M., Trayner, P.M., Trimble, T.J., 1988. Mesozoic reactivation of Variscan thrusting in the Bristol Channel area, U.K. J. Geol. Soc. Lond. 145, 439–444.

Bürgmann, R.D., Pollard, D., Martel, S.J., 1994. Slip distributions on faults: effects of stress gradients, inelastic deformation, heterogeneous host-rock stiffness, and fault interaction. J. Struct. Geol. 16, 1675–1690.

Chadwick, R.A., 1986. Extension tectonics in the Wessex Basin, southern England. J. Geol. Soc. Lond. 143, 444–465.

Chinnery, M.A., 1961. The deformation of ground around surface faults. Bull. Seism. Soc. Am. 51, 355–372.

Comninou, M.A., Dunders, J., 1975. The angular dislocation in a half-space. J. Elasticity 5, 203–216.

Coulomb, C.A., 1773. Sur une application des règles de Maximis et Minimis à quelques problèmes de statique relatifs à l'Architecture. Acad. Roy. Des Sciences Mémoires de math. Et de physique par divers savants 7, 343–382.

Cowie, P.A., Scholz, C.H., 1992. Growth of faults by accumulation of seismic slip. J. Geophys. Res. 97, 11,085–11,095.

Cowie, P.A., Shipton, Z.K., 1998. Fault tip displacement gradients and process zone dimensions. J. Struct. Geol. 97 (1), 983–997.

Crider, J.G., Pollard, D.D., 1998. Fault linkage: three dimensional mechanical interaction between echelon normal faults. J. Geophys. Res. 103, 24,373–24,391.

Engelder, T., 1985. Loading paths to joint propagation during a tectonic cycle: an example from the Appalachian plateau, USA. J. Struct. Geol. 7, 459–476.

Engelder, T., 1987. Joints and shear fractures in rock. In: Atkinson, B.K. (Ed.). Fracture Mechanics of Rock. Academic Press Geology Series, pp. 27–69.

Griffith, A.A., 1924. Theory of rupture. In: First International Congress Applied Mechanics, Delft, pp. 55–63.

Hancock, D.L., 1985. Brittle microtectonics: principles and practice. J. Struct. Geol. 7 (3/4), 437–457.

Harris, J.F., Taylor, G.L., Walper, J.L., 1960. Relation of deformational fractures in sedimentary rocks to regional and local structures. A.A.P.G. Bulletin 44, 1853–1873.

Holzhauzen, G.R., Johnson, A.M., 1979. The concept of residual stress in rock. Tectonophysics 58, 237–267.

Hyett, A.I., Hudson, J.A., 1990. A photo-elastic investigation of the stress state close to rock joints. In: Barton, N., Stephansson, O. (Eds.), Intl. Symp. on Rock Joints. Balkema, Rotterdam, pp. 227–233.

Jeyakumaran, M., Rudnicki, J.W., Keer, L.M., 1992. Modeling slip zones with triangular dislocation elements. Seis. Soc. Am. Bull. 82, 2153–2169.

Lewis, C., Davis, T.L., Vuillermoz, C., Gurch, M., Iverson, W.-P., Schipperijn, A.P., 1990. Three-dimensional multicomponent imaging of reservoir heterogeneity, Silo Field, Wyoming. In: Society of Exploration Geophysicists, 59th Ann. Int. Meeting, pp. 763–766.

Lisle, R.J., 1994. Detection of zones of abnormal strains in structures using Gaussian curvature analysis. A.A.P.G. Bulletin 78, 1811–1819.

Martel, J.S., Boger, W.A., 1998. Geometry and mechanics of secondary fracturing around small three-dimensional faults in granitic rock. J. Geophys. Res. 103 (B9), 21,299–21,314.

Martel, S.J., 1997. Effects of cohesive zones on small faults and implications for secondary fracturing and fault trace geometry. J. Struc. Geol. 19, 835–847.

McLachlan, A.C., 1986. A revised interpretation of the structures within the Mesozoic of North-West Somerset. Unpublished Masters dissertation thesis, Imperial College.

Mohr, O., 1900. Welche Umstände bedingen die Elastizitätsgrenze und den Bruch eines Materials. Z. Ver. Dt. Ing. 44, 1524–1530 also 1572–1577.

Mohr, O., 1914. Abhandlungen aus dem Gebiete der technische Mechanik. Ernst und Sohn, Berlin.

Narr, W., Currie, J.B., 1982. Origin of fracture porosity. A.A.P.G. Bulletin 66, 1231–1247.

O'Connel, R.J., Budiansky, B., 1977. Visco-elastic properties of fluid-saturated and cracked solids. J. Geophys. Res. 82, 5719–5735.

Okada, Y., 1985. Surface deformation due to shear and tensile faults in a half-space. Bull. Seis. Soc. Am. 75 (4), 1135–1154.

Peacock, D.C.P., Sanderson, D.J., 1992. Effects of layering and anisotropy on fault geometry. J. Geol. Soc. Lond. (149), 793–802.

Petit, J.P., Auzias, V., Rawnsley, K., Rives, T. 2000. Development of joint sets in association with faults. In: Lehner, F.K., Urai, J.L. (Eds.). Aspects of tectonic failing — in honour of Georg Mandl. Springer, Berlin.

Pollard, D.D., Segall, P., 1987. Theoretical displacements and stresses near fractures in rock: with applications to faults, joints, veins, dikes, and solution surfaces. In: Atkinson, B.K. (Ed.). Fracture Mechanics of Rock. Academic Press, London, pp. 277–349.

Price, N.J., 1966. Fault and Joint Development in Brittle and Semi-brittle Rock. Pergamon, Oxford.

Rawnsley, K.D., Rives, T., Petit, J.P., Hencher, S.R., Lumsden, A.C., 1992. Joint development in perturbed stress fields near faults. J. Struct. Geol. 14, 939–951.

Rawnsley, K.D., Peacock, D.C.P., Rives, T., Petit, J.P., 1998. Joints in the Mesozoic sediments around the Bristol Channel Basin. J. Struct. Geol. 20 (12), 1641–1661.

Rispoli, R., 1981. Stress fields around strike-slip faults inferred from stylolites and tension gashes. Tectonophysics 75, T29–T36.

Rodgers, D.A., 1980. Analysis of pull-apart basin development produced by en echelon strike-slip faults. Spec. Publ. Int. Assoc. Sedimentol. 4, 27–41.

Rongved, L., Frasier, J.T., 1958. Displacement discontinuity in an elastic half-space. J. Appl. Mech. 25, 125–128.

Scholz, C.H., Dawers, N.H., Yu, J.Z., Anders, M.H., 1993. Fault growth and fault scaling laws: preliminary results. J. Geophys. Res. 98, 21,951–21,961.

Segall, P., Pollard, D.D., 1980. Mechanics of discontinuous faults. J. Geophys. Res. 85, 4337–4350.

Stearns, D.W., 1964. Macrofracture patterns on Teton Anticline, northwestern Montana. Am. Geophys. Union Trans. 45, 107–108.

Steketee, J.A., 1958. On Volterra's dislocation in a semi-infinite elastic medium. Can. J. Phys. 36, 192–205.

Thomas, A.L., 1993. Poly3D: A three-dimensional, polygonal element, displacement discontinuity boundary element computer program with applications to fractures, faults, and cavities in the Earth's crust. Unpublished M.Sc. dissertation thesis, Stanford University, California.

Turcotte, D.L., Schubert, G., 1982. Geodynamics: Application of Continuum Physics to Geological Problems. Wiley, New York.

Weibull, W., 1939. A statistical theory of the strength of materials. Ingvetensk. Akad. Handl., 149.

Willemse, E.J.M., 1997. Segmented normal faults: Correspondence between three-dimensional mechanical models and field data. J. Geophys. Res. 102, 675–692.

Willemse, E.J.M., Pollard, D.D., 1998. On the orientation and pattern of wing cracks and solution surfaces at the tips of a sliding flaw or fault. J. Geophys. Res. 103, 2427–2438.

Willemse, E.J.M., Pollard, D.D., Aydin, A., 1996. Three-dimensional analyses of slip distributions on normal fault arrays with consequences for fault scaling. J. Struct. Geol., 295–309.

Zoback, M.D., Zoback, M.L., Mount, V.S., Suppe, J., Eaton, J.P., Healey, J.H., Oppenheimer, D., Reasenberg, P., Jones, L.M., Raleigh, C.B., Wong, I.G., Scotti, O., Wentworth, C., 1987. New evidence on the state of stress on the San Andreas fault system. Science 238, 1105–1111.